Semi-Autonomous 2.5D Control of Untethered Magnetic Suture Needle

Qinhan Wang[1], Anuruddha Bhattacharjee[1], Xinhao Chen[1,2], Lamar O. Mair[3], Yancy Diaz-Mercado[4], and Axel Krieger[1,2*]

***Abstract*— Untethered miniature surgical tools could significantly reduce invasiveness and enhance patient outcomes in robot-assisted laparoscopic surgical procedures. This paper demonstrates the feasibility of performing semi-autonomous suturing tasks using an untethered magnetic needle controlled by an external electromagnetic manipulator. The electromagnetic manipulator can generate magnetic torques and gradient-based pulling forces to actuate the magnetic needle. Here, we develop and implement a semi-autonomous 2.5D control method for controlling the in-plane position and both in-plane and out-of-plane orientations of a magnetic needle for suturing on tissue-mimicking agar gel phantoms. The method includes recognizing needles and incisions, planning trajectory, and performing suturing with visual feedback control. We conduct two mock suturing tasks using both continuous and interrupted techniques on 1% agar gel phantoms with 2 cm and 3 cm incision sizes. The results demonstrate precise needle control, with an average root-mean-square position error of 1.01 mm and 1.12 mm across tasks. The system also achieved submillimeter-level suture spacing accuracy, comparable to surgeons using state-of-the-art surgical robots. These findings highlight the feasibility of using untethered magnetic suture needles for minimally invasive suturing procedures.**

I. Introduction

Robot-assisted minimally invasive surgery (MIS) has revolutionized surgical practices by allowing complex procedures through small incisions or natural orifices [1], which reduces tissue damage, accelerates recovery, and minimizes post-operative infections and discomfort [2]–[4]. Suturing and ligation inside the body are crucial yet challenging aspects of these procedures, demanding precise control in confined spaces [5]. While recent developments in surgical robotic systems have demonstrated enhanced precision with advanced vision feedback [5] and planning [6], they still require large manipulators that occupy significant space inside the patient, increasing the risks of unwanted tissue damage, scarring, and infection [7], [8]. Addressing these issues remains a key goal in advancing surgical robotics. Especially for intraperitoneal bladder wall lacerations during laparoscopic surgery, commonly repaired by intracorporeal suturing laparoscopically or an exploratory laparotomy, which demand less invasive suture procedures [9].

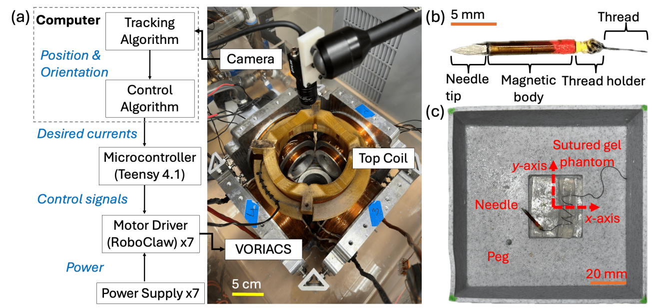

Fig. 1. (a) The electromagnetic system and camera. (b) Magnetic suture needle. (c) Overview of the workspace, sutured sample, and the needle.

Magnetic manipulation presents a promising advancement for robot-assisted MIS to further reduce invasiveness by enabling untethered guidance of magnetic surgical tools (i.e., suture needles) inside the human body [10], [11]. Magnetic suture needles with attached threads can be wirelessly guided by external magnetic fields to perform tissue penetration, suturing, and ligation tasks [12]. Previous works in this domain have demonstrated innovative magnetic needle designs with excellent manipulation capability for different tasks, including 2D teleoperation for tissue suturing and ligation [12], autonomous 2D navigation [13], autonomous 2D localization and control in environments with blood and tissue [14], 2D teleoperation for *ex-vivo* tissue suturing [15], and 2D teleoperation of impact-based hammer needle for tissue penetration [16] and tissue mimic suturing [17].

Despite recent advancements, most existing studies restrict needles to two-dimensional planar motions, reducing their effectiveness in realistic surgical scenarios. Moreover, no research has demonstrated autonomous suturing using a tetherless magnetic needle. Motivated by clinical needs and research gaps, this study presents a visual feedback-based approach for semi-autonomous 2.5-dimensional (2.5D) control of an untethered magnetic suture needle. The system is designed for suturing tasks in tissue-mimicking gel phantoms, simulating a scenario where a small endoscopic camera and a magnetic needle are used in the aquatic environment of the intraperitoneal bladder. By integrating a top (z-axis) electromagnetic coil with a planar (x-y plane) electromagnetic manipulation system and a visual feedback method, semi-autonomous 2.5D control of both position and in-plane or out-of-plane orientation of a magnetic needle

This work was supported by the National Science Foundation's Foundational Research in Robotics CAREER program under award number 2144348.

[1]Laboratory for Computational Sensing and Robotics, Johns Hopkins University, Baltimore, MD 21218, USA. Email: {qwang148, abhatt27, xchen254, axel}@jhu.edu.

[2]Department of Mechanical Engineering, Johns Hopkins University, Baltimore, MD 21218, USA.

[3]Division of Magnetic Manipulation and Particle Research, Weinberg Medical Physics, MD 20852, USA. Email: lamar.mair@gmail.com.

[4]Department of Mechanical Engineering, University of Maryland, College Park, MD 20742, USA. Email: yancy@umd.edu.

*Corresponding author

could be achieved. Using this method, we demonstrate the feasibility of performing continuous and interrupted suturing tasks in phantoms with varying incision sizes. This control strategy for suture needles holds promise for autonomously maneuvering around tissues or organs to execute out-of-plane stitches for the first time, facilitating the deployment of untethered magnetic needles in robot-assisted surgeries.

The paper is organized as follows: Section II introduces the electromagnetic robotic surgical manipulator and the experimental testbed. Section III explains the dynamic model for actuating the magnetic needle. Section IV elaborates on the control methods utilized in our experiments. Section V shows the two suture tasks completed and analyzes their results. Finally, Section VI concludes the paper by summarizing our achievements and discussing potential improvements.

II. Magnetic Surgical System

Our magnetic surgical system includes an electromagnetic manipulation system, magnetic surgical tools (e.g., magnetic needles), tissue-mimicking gel samples in a 3D-printed workspace, and a digital camera for visual feedback. The following sections describe all the system's components.

A. Electromagnetic Manipulation System

In this study, a 12-coil planar electromagnetic system (VORIACS: Variable Outer Radius Individually Addressable Coil System) along with a top coil for out-of-plane control is utilized to generate external magnetic fields and manipulate magnetic needles for surgical tasks. The VORIACS system consists of four coil stack units, with each unit containing three concentric coils with variable outer radii, surrounding a $100 \times 100 \times 100$ mm^3 center workspace. Detailed specifications of the VORIACS system can be found in [18], [19]. In addition to the 12 planar coils, a top coil is positioned 10 cm above the workspace plane, as shown in Fig. 1(a). All 12 planar coils in the VORIACS system are independently controlled by six motor drivers (Roboclaw, 2x60AHV) operating in two-channel mode. The six motor drivers are powered by six power supplies (SL Power, TF3000A60K) rated at 60 V and 50 A. The top coil is individually controlled and powered by a seventh motor driver and a 24 V power supply, which can generate up to 4 miliTesla at the center of the workspace. A dedicated CPU (i7-13700KF) running a custom MATLAB script interfaces with the motor drivers through a Teensy microcontroller. The microcontroller starts the motor drivers using pulse width modulation signals to power the coils.

B. Magnetic Suture Needle

1) Needle design and fabrication: The electromagnetic system can exert magnetic forces and torques on any magnetic needle to penetrate and steer it through tissue for a suturing task. The applied magnetic force on a needle is described by $\mathbf{F}_m = \mathbf{m} \cdot \nabla \mathbf{B}$, where $\boldsymbol{m}$ denotes the magnetic dipole moment vector of the magnetic agent, and $\nabla \mathbf{B}$ is the magnetic field gradient of the electromagnets. Commercially available stainless steel suture needles are soft magnetic (e.g., their magnetization changes with the applied magnetic field), have a low magnetization, and may require a significantly large magnetic field gradient to generate the required forces for tissue penetration. Alternatively, a needle with neodymium iron boron (NdFeB) permanent magnets could have a strong magnetization and may be suitable for suturing tasks with our electromagnetic system. Therefore, we have designed a custom magnetic needle consisting of a sharp stainless steel needle tip (diameter 1.6 mm) attached to a polyimide tube (inner diameter: 1.7 mm, wall thickness 0.032 mm) with embedded two cylindrical neodymium permanent magnets (each with 1.5 mm diameter, 5 mm height, and magnetic dipole moment of 0.00989 Am^2). A 3D-printed part with a closed thread eye is also attached at the tail of the needle to hold a 6-0 silk suture thread. Fig. 1(b) shows the needle and its components.

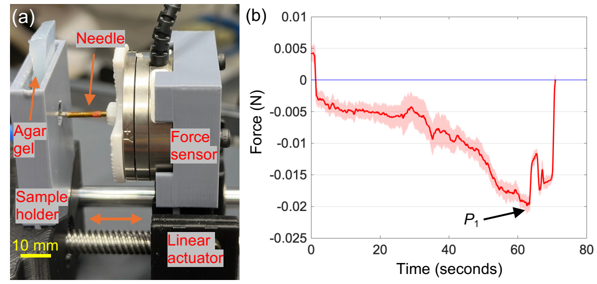

Fig. 2. (a) Force measurement setup. (b) Representative penetration force measurement data for 1.0% agar gel sample. P_1 indicates the puncture point for the magnetic needle. The red-colored solid line and the shaded area represent the mean and standard deviation of the force data, respectively.

2) Tissue-mimic penetration force assessment: Suturing a tissue or tissue-mimicking sample would require penetrating it with a suture needle and pulling the needle through it. To evaluate the penetration forces for pulling the customized magnetic needle through tissue-mimicking agar gel samples, we conduct force tests using a force measurement setup as shown in Fig. 2(a). In the setup, a magnetic needle is attached to a force and torque sensor (F/T Sensor: mini40, calibration: SI-20-1 calibration, ATI Industrial Automation) with 3D-printed fixtures, and the sensor is attached to a motorized linear actuator that maintains a constant speed while pushing the needle through agar gel samples. Agar gel samples with 1.0% (comparable elastic modulus [20] to human bladder wall [21]) and 1.5% (mimics gastric tissue [22]) are prepared (i.e., dissolving 1 gram and 1.5 grams of agarose powder in 100 mL deionized water yields 1.0% and 1.5% agar gels, respectively) and utilized for the tests. Using a data acquisition (DAQ) system (myRIO-1900, National Instruments), we measure forces on the needle at 10 Hz frequency while inserting the needle through agar gel samples until a complete penetration is achieved.

Fig. 2(b) shows the force exerted on a magnetic needle as a function of time during the penetration of a 4 mm thick, 1.0% agar gel sample. Upon initial contact with the gel, the needle experiences a rebound force, as indicated by positive force values in the plot. As the needle starts penetrating the sample, the resistive force (acting in the opposite direction of the needle's motion) increases, reaching a negative peak at the puncture point (P_1). Three samples of both 1.0% and 1.5% agar gel are tested. The mean puncture force for the 1.0% agar gel is 19.75 millinewton (mN), with a standard deviation of 2.29 mN, while the 1.5% agar gel shows a mean puncture force of 45.43 mN and a standard deviation of 5.90 mN. Using the magnetic field data and needle magnet properties, we calculate the maximum pulling force the system can apply at the center of the workspace to be 24.86 mN. This force is sufficient for penetrating the 1% agar gel but is inadequate for the 1.5% agar gel. Consequently, we select the 1.0% agar gel for preparing tissue-mimicking phantoms.

C. Tissue-Mimicking Agar Gel Phantom and Workspace

To accurately simulate suture scenarios, we design and fabricate tissue-mimicking agar gel phantoms in a 3D-printed workspace that mimics the typical shape of a tissue with incision, as shown in Fig. 1(c). The 40 mm high 3D-printed workspace features a 100×100 mm^2 square-shaped box with a peg at the bottom-left corner and a central rectangular cavity for positioning the agar gel phantom.

The agar gel phantom, featuring a central groove representing an incision, is composed of 1.0% agar. This concentration is achieved by dissolving agarose powder in water at a weight-to-volume ratio of 1:100. The solution is heated to boiling temperature to ensure complete dissolution before the mixture is poured into a custom 3D-printed mold. After cooling to room temperature, the polymerized agar gel is removed from the mold and affixed within the cavity using super glue. Finally, the workspace is filled with pure glycerin to submerge the agar to simulate an aquatic environment of the intraperitoneal bladder wall.

D. Vision Feedback and Needle Tracking

Autonomous manipulation of a magnetic needle requires continuous and precise tracking of both its position and orientation. In our system, a vertically mounted top digital camera (BFS-U3-13Y3, FLIR) provides constant visual feedback, while a MATLAB script implementing an HSV color filter-based tracking algorithm allows tracking the orange and red colored segments of the needle's body, which represent the front and back ends, respectively. By tracking these two colored areas, the algorithm calculates their centroids and connects them with a line. The midpoint of this line defines the needle's centroid, while the orientation of the line corresponds to the needle's planar orientation. Given the strong magnetization of the needle, which aligns with the externally applied magnetic field, its out-of-plane orientation can be estimated based on the direction of the applied magnetic field. This method allows accurate tracking of both the in-plane position and in-plane or out-of-plane orientation of the magnetic needle, enabling its autonomous manipulation.

III. Dynamic Model of Magnetic Actuation

A gradient magnetic field exerts both force and torque on a magnetic agent. In this study, the magnetic needle contains small permanent magnets located at the center of its body, acting as a magnetic agent. The force $\boldsymbol{F}$ is discussed earlier, and the torque $\boldsymbol{T}$ acting on the magnetic needle is given by

$$\boldsymbol{T} = \boldsymbol{m} \times \boldsymbol{B}, \tag{1}$$

where $\boldsymbol{B}$ is the magnetic field vector, which scales linearly with applied currents.

The navigation of the magnetic needle in the x-y plane is controlled using eight electromagnetic coils, and the relationship between the forces, torques, and associated coil currents is described by

$$\begin{bmatrix} F_x \\ F_y \\ \boldsymbol{T} \end{bmatrix} = \begin{bmatrix} \boldsymbol{m}^T \begin{bmatrix} \frac{\partial \widetilde{\boldsymbol{B_1}}}{\partial x} \frac{\partial \widetilde{\boldsymbol{B_2}}}{\partial x} \cdots \frac{\partial \widetilde{\boldsymbol{B_8}}}{\partial x} \end{bmatrix} \\ \boldsymbol{m}^T \begin{bmatrix} \frac{\partial \widetilde{\boldsymbol{B_1}}}{\partial y} \frac{\partial \widetilde{\boldsymbol{B_2}}}{\partial y} \cdots \frac{\partial \widetilde{\boldsymbol{B_8}}}{\partial y} \end{bmatrix} \\ \boldsymbol{m} \times \begin{bmatrix} \widetilde{\boldsymbol{B_1}} \widetilde{\boldsymbol{B_2}} \ldots \widetilde{\boldsymbol{B_8}} \end{bmatrix} \end{bmatrix} \begin{bmatrix} I_1(t) \\ I_2(t) \\ \vdots \\ I_8(t) \end{bmatrix}, \tag{2}$$

where F_x and F_y are the forces along the x- and y-directions, $\widetilde{\boldsymbol{B_i}}$ is the current-normalized magnetic field generated by the ith electromagnetic coil, and I_i is its corresponding current. An additional top coil positioned directly above the workspace and oriented along the z-axis of the workspace facilitates open-loop controlled in-plane and out-of-plane manipulations. When activated, this coil induces the sharpened tip of the needle to tilt either upwards or downwards as it attempts to align with the magnetic field direction produced by the top coil. Together with the other eight coils placed along the x-y plane for horizontal actuation, this configuration enables the needle to exhibit 2.5D manipulability. This allows the needle to navigate obstacles such as an uneven agar surface, mimicking the challenges of uneven tissue surfaces and elevated incision gaps in surgical settings. However, magnetic forces and torques from the top coil are not included in (2), as the top coil is under open loop control, which does not contribute to the closed-loop dynamics and will be explained in later sections.

The magnetic needle is sufficiently light and surrounded by sufficiently low viscosity fluid, to enable quick alignment with the magnetic field direction, eliminating the need to consider torque in this study. As a result, (2) can be further simplified to (3) as

$$\begin{bmatrix} F_x \\ F_y \\ \omega_o \cdot B_x \\ \omega_o \cdot B_y \end{bmatrix} = \begin{bmatrix} \boldsymbol{m}^T \begin{bmatrix} \frac{\partial \widetilde{\boldsymbol{B_1}}}{\partial x} \frac{\partial \widetilde{\boldsymbol{B_2}}}{\partial x} \cdots \frac{\partial \widetilde{\boldsymbol{B_8}}}{\partial x} \end{bmatrix} \\ \boldsymbol{m}^T \begin{bmatrix} \frac{\partial \widetilde{\boldsymbol{B_1}}}{\partial y} \frac{\partial \widetilde{\boldsymbol{B_2}}}{\partial y} \cdots \frac{\partial \widetilde{\boldsymbol{B_8}}}{\partial y} \end{bmatrix} \\ \widetilde{B}_{1x} \widetilde{B}_{2x} \ldots \widetilde{B}_{8x} \\ \widetilde{B}_{1y} \widetilde{B}_{2y} \ldots \widetilde{B}_{8y} \end{bmatrix} \begin{bmatrix} I_1(t) \\ I_2(t) \\ \vdots \\ I_8(t) \end{bmatrix}, \tag{3}$$

where B_x and B_y form the unit vector of the desired direction. The $\widetilde{B}_{ix}$ and $\widetilde{B}_{iy}$ are the components of $\widetilde{\boldsymbol{B_i}}$ along the x- and y-axes, respectively. We can express (3) as $\boldsymbol{C} = \boldsymbol{AI}$, where (3) builds a mapping from the desired force and direction to the input currents through matrix $\boldsymbol{A}$. This matrix bases on the linear relationship between input currents of all coils and the magnetic field $\boldsymbol{B}$ and its gradient $\nabla \boldsymbol{B}$ at all points within the workspace. This relationship has been established in our previous study [19] through finite element analysis. We solve (3) using the method of singular value decomposition (SVD) and a singularity solver [19], which allows controlling the needle in closed-loop by dynamically adjusting the input currents to all coils.

IV. Semi-autonomous 2.5D Control Method

Our control method includes recognizing incisions, planning waypoints and penetration points, and performing suturing with 2.5D maneuvers under visual feedback control. At the beginning of each suture task, the incision within the workspace is recognized, with waypoints and penetration points specified by the path planning algorithm. Under visual feedback control, the needle then operates in navigation mode to approach these waypoints and switches to penetration mode to penetrate the gel phantom at the penetration points. Pulling mode is subsequently activated to extract the thread from the gel phantom. The functionality of each mode will be detailed in the following subsections.

A. Incision Recognition and Path Planning

We utilized a pre-trained Segment Anything Model (SAM) [23] implemented in MATLAB to identify incisions within the workspace, guided by a human operator. At the start of each suturing session, the system captures a snapshot of the workspace. The operator then selects the region of interest, prompting SAM to segment and highlight the identified incision for the operator to either approve or request a re-segmentation based on their assessment. Upon approval, our path planning algorithm takes over and generates a trajectory that distributes suture points evenly across the incision based on the task type and the detected incision shape.

B. Navigation Mode

For needle guidance in liquid, an optimized closed-loop control approach using 8 coils out of 12 coils is implemented to prevent redundant power burden and overheating of coils. A standard PID controller is used to compute the desired forces acting on the needle, while the desired field direction is determined directly from the desired orientation of the needle. The forces and fields in (3) can be derived from (4) by

$$\begin{bmatrix} F_x \\ F_y \end{bmatrix} = k_p \cdot \boldsymbol{e} + k_i \cdot \int \boldsymbol{e} dt + k_d \cdot \dot{\boldsymbol{e}}, \quad \begin{bmatrix} B_x \\ B_y \end{bmatrix} = \begin{bmatrix} \sin(\theta_{des}) \\ \cos(\theta_{des}) \end{bmatrix}, \tag{4}$$

where $\boldsymbol{e}$ is the vector from the needle's current position to the desired position. θ_{des} is the desired orientation, and $\boldsymbol{k}_p$, $\boldsymbol{k}_i$, and $\boldsymbol{k}_d$ are 5.5, 0.1, and 1, respectively, with a unit of 10^{-4} to compensate the difference in units conversion during calculations. The navigation mode operates at 22% of the maximum current capacity, which is sufficient for moving the needle both freely and precisely within the workspace.

C. Penetration Mode

In penetration mode, the top z-axis coil and all three coils on one side are activated at 60% and 95% of their maximum current capacity, respectively. This configuration provides control over the needle's out-of-plane orientation and delivers the maximum penetration force while maintaining system stability and preventing overheating. Once the needle aligns with the designated penetration points, the operator directs the control system to switch to penetration mode, enabling the completion of the gel phantom penetration process while ensuring both system and procedural safety.

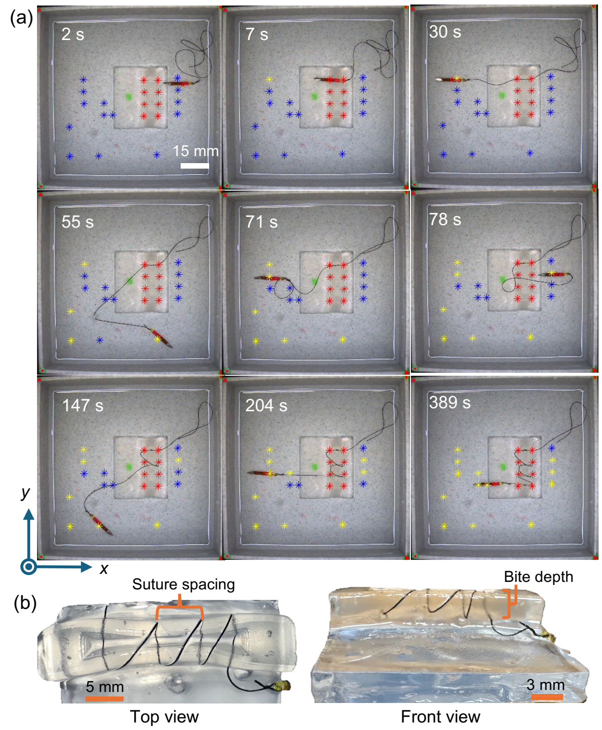

Fig. 3. (a) Video snapshots showing suturing a 2 cm incision with a single magnetic needle. (b) Top and front views of the sutured tissue-mimic gel sample with suture spacing and bite depth measurement.

D. Pulling Mode

In the pulling mode, the system uses the same PID controller as the navigation mode but with 47% of maximum current capacity to efficiently extract the thread from the phantom and tighten the stitches while maintaining precise needle movement. Additionally, the top z-axis coil is activated for maneuvering the uneven surface of the incision.

V. Experiments and Results

We design two distinct suture scenarios to mimic real surgical scenarios with varied incision sizes. Task 1 simulates the suturing repair of a bladder wall intraperitoneal injury featuring an incision size of 2 cm. Such an incision requires a single-layer closure using a running non-locked stitch with a single needle [9]. On the other hand, Task 2 tackles a larger incision size of 3 cm, which could have broader applications in surgical repairs. The results from the two suturing tasks are described in detail in the following sections.

A. Task 1: Small Incision Suturing with Single Needle

Fig. 3(a) shows video snapshots of the suturing Task 1, where a 1% agar gel phantom, mimicking a bladder wall injury with a 2 cm incision, is sutured using a single needle in four continuous stitches. After the first stitch, the needle

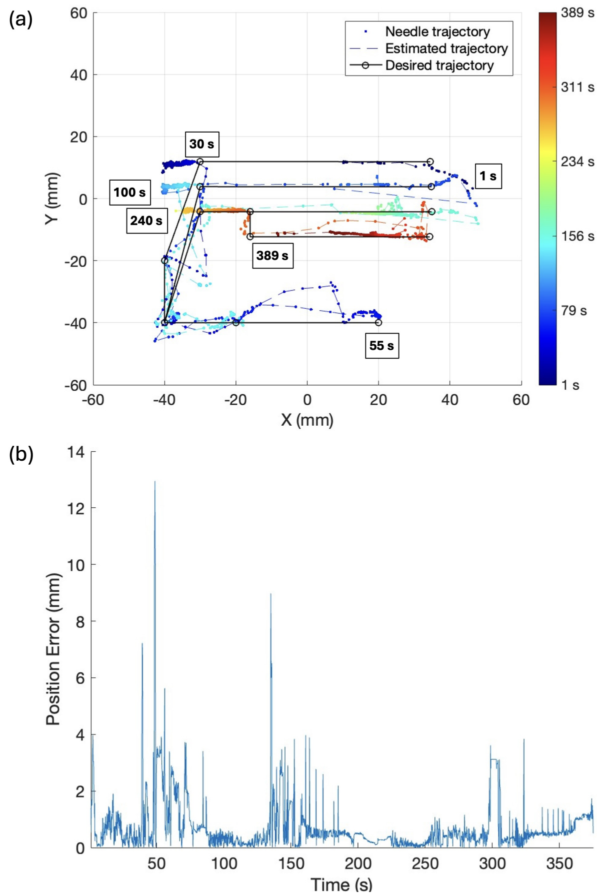

Fig. 4. (a) Magnetic needle's actual trajectory (colored dots) along with the estimated trajectory (dashed line) compared to the desired trajectory (black solid line) for a small incision suturing with a single needle. (b) Position error vs time plot for the small incision suturing with a single needle.

maneuvers around the peg to a distant point (see Fig. 3(a) at 55 s), simulating the looping of thread around the scope to pull enough thread for subsequent stitches. Following the second stitch, the needle circles the peg again to tighten the stitch (see Fig. 3(a) at 147 s).

The suture needle's actual trajectory compared to the desired trajectory for Task 1 is visualized in Fig. 4(a) using colored dots to denote the temporal sequence of movements. Note that due to the camera's limited frame rates (30 fps), consecutive recorded positions of the needle may appear significantly separated. This typically occurs when the needle moves too rapidly, such as exiting the sample after completing a stitch. In these instances, trajectories are estimated by connecting consecutive distant points with dashed lines. The desired trajectory of the magnetic suture needle, composed of multiple waypoints, is depicted as a thin black solid line in Fig. 4(a) with waypoints marked in circles.

Fig. 4(b) illustrates the trajectory tracking position error of the needle during Task 1 throughout a suturing session. The average root-mean-square (ARMS) position error of the needle for Task 1 was 1.01 mm across three trials. Notably, the two sharp spikes in the error magnitude were caused by the counterforce exerted by the thread during its extraction from the sample. This unexpected counterforce can lead to sudden deviations from the needle's desired path.

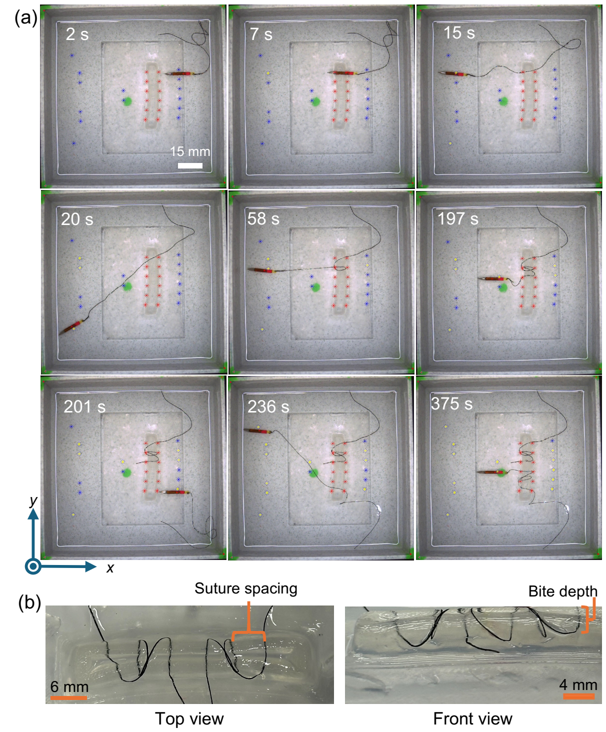

Fig. 5. (a) Video snapshots showing suturing a 3 cm incision with two magnetic needles. (b) Top and front views of the sutured tissue-mimic gel sample with suture spacing and bite depth measurement.

B. Task 2: Large Incision Suturing with Two Needles

Task 2 uses the interrupted stitching technique for larger incisions that require multiple sutures to effectively manage closure when a single suture thread is insufficient. Initially, a needle and thread are used to complete the first three stitches. Upon completion, we remove the first needle, leaving the thread in place to continue closing the incision. A new needle with thread is then introduced to perform the remaining three stitches, as shown in Fig. 5. Each needle in Task 2 is also directed to a diagonal far point after the first stitch to ensure sufficient thread is pulled out to complete the remaining planned stitches (see Fig. 5 at 20 s and 236 s).

Fig. 6(a) shows the needle's actual, estimated, and desired trajectories for one of the three test sessions conducted for Task 2. The tests conclude with an ARMS position error of 1.12 mm across three test sessions. The primary contributors to this error were the thread pulling and the positional discrepancy between the entry point of the second needle in the workspace and its initially designated waypoint.

C. Suturing Task Assessment

Three tests are conducted for each suturing task to assess the consistency and accuracy of the suture outcomes using two primary evaluation metrics: suture spacing and bite depth. Suture spacing refers to the distance between consecutive entry and exit points of the incision and is measured per

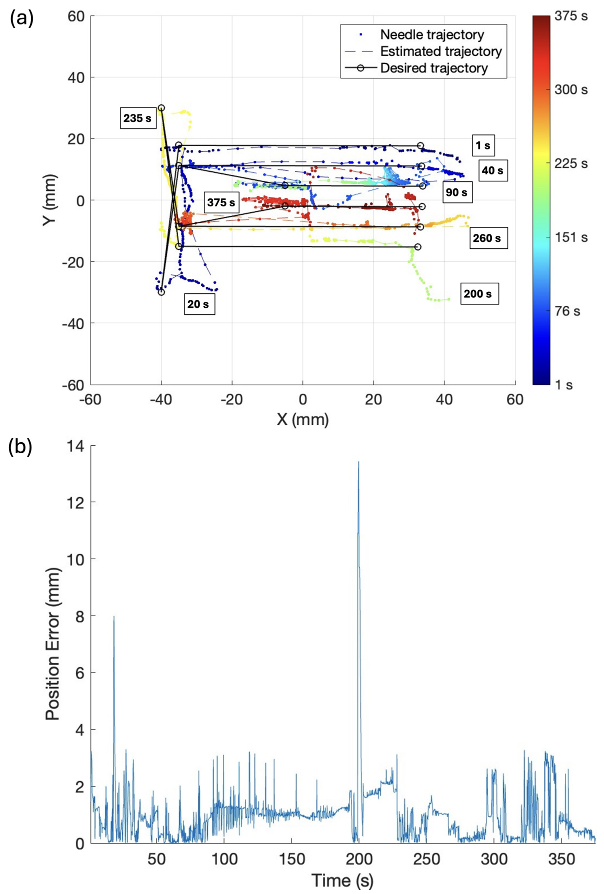

Fig. 6. (a) Magnetic needle's actual trajectory (colored dots) along with the estimated trajectory (dashed line) compared to the desired trajectory (black solid line) for a large incision suturing with two needles. (b) Position error vs time plot for the large incision suturing with two needles.

stitch in the tasks. Bite depth is defined as the distance from the suture entry point to the tissue edge and is also measured per stitch (see Fig. 3(b) and Fig. 5(b)). The accuracy of the suturing is evaluated based on the mean values of suture spacing and bite depth, while the standard deviation (Std) of these measurements determines consistency. The results from these evaluations are presented in Table I. For both suturing tasks, the planned suture spacing was 6 mm. For Task 1, the mean spacing error is 0.35 mm (5.83% of the planned suture spacing) with a standard deviation of 1.51 mm. For Task 2, the mean spacing error is 0.81 mm (13.5% of the planned suture spacing) with a standard deviation of 1.29 mm. Compared to the standard deviations of suture spacing achieved by human surgeons using continuous suture techniques with laparoscopic suturing and the autonomous STAR system [5], as shown in Table I, the standard deviation of the suture spacing from our magnetic system shows only submillimeter differences. Moreover, the mean bite depth with our magnetic system for Task 1 and Task 2 were 4.95 mm and 4.12 mm with a standard deviation of 0.51 mm and 0.55 mm, respectively. This indicates a level of consistency comparable to these established methods [5]. Note that due to the limitations of visual tracking, several inevitable sources

TABLE I
QUANTITATIVE ASSESSMENT OF SUTURING TASKS

Suture Spacing (mm)			
Suturing Tasks	Magnetic System Mean±Std	Laparoscopic Mean±Std	STAR [5] Mean±Std
Task 1	5.65±1.51 (n = 12)	2.282±1.035	3.049±0.8039
Task 2	5.19±1.29 (n = 15)	NA	NA
Bite Depth (mm)			
Task 1	4.94±0.51 (n = 16)	2.023±1.101	3.05±0.9148
Task 2	4.12±0.55 (n = 18)	NA	NA

of error arise, including distortions and visual misalignment. These errors are mostly caused by the deformation of the agar gel sample, refraction from the viscous liquid, and the depth variations between the incision top and the suture plane.

VI. Discussion and Conclusion

This paper presents a semi-autonomous, vision-guided control method for untethered magnetic suture needles, demonstrating its promise in enhancing surgical operations, particularly in the repair of bladder wall injuries. The proposed method demonstrated precise and consistent suturing results in tissue-mimicking gel phantoms. In real-world surgical environments with human-sized workspaces, adopting larger coil systems with MRI-similar configurations could overcome some current limitations. Specifically, these systems could produce stronger electromagnetic fields to generate sufficient force for suturing diverse tissues while keeping the tools miniaturized and ensuring the safety of surrounding areas. Additionally, while effective for basic operations, the PID controller struggles with error handling, especially against unexpected external forces such as the counterforce from the thread, which was a major source of position error and suture time variance in our experiments.

Future work could include establishing a precise model of various needles and threads for enhanced control accuracy and effectiveness. Furthermore, to transition toward real surgical suture operations, learning-based approaches can be adopted to both overcome the limitations of color tracking and generate high-level policies for intelligent decision-making in complex surgical environments. Additionally, performing studies on real tissues would refine the system's responsiveness to realistic surgical conditions, paving the way toward fully autonomous surgical procedures.

Our experiments have underscored the potential of electromagnetically actuated needles in facilitating less invasive suture procedures. Employing a hybrid control method that allows for predominantly autonomous manipulation, we have demonstrated the precise accuracy and consistency of our magnetically actuated suture needle across two suture tasks and incision lengths. This work marks another step toward fully autonomous surgical procedures.

Acknowledgment

We thank Noah Barnes, Lingyun Di, and Lidia Al-Zogbi for helping us with the force measurement setup and 3D printing.

REFERENCES

[1] R. S. Chamberlain and S. V. Sakpal, "A comprehensive review of single-incision laparoscopic surgery (sils) and natural orifice transluminal endoscopic surgery (notes) techniques for cholecystectomy," *Journal of Gastrointestinal Surgery*, vol. 13, no. 9, pp. 1733–1740, 2009.

[2] C. Tsui, R. Klein, and M. Garabrant, "Minimally invasive surgery: national trends in adoption and future directions for hospital strategy," *Surg. Endosc.*, vol. 27, pp. 2253–2257, 2013.

[3] L. Ma, H. Luo, S. Kou, Z. Gao, D. Bai, X. Qin, T. Ouchi, L. Gong, J. Hu, and Y. Tian, "Robotic versus laparoscopic surgery for hiatal hernia repair: a systematic literature review and meta-analysis," *J. Robot. Surg.*, vol. 17, no. 5, pp. 1879–1890, 2023.

[4] J. A. R. de Vermandois, G. Cochetti, M. D. Zingaro, A. Santoro, M. Panciarola, A. Boni, M. Marsico, G. Gaudio, A. Paladini, P. Guiggi *et al.*, "Evaluation of surgical site infection in mini-invasive urological surgery," *Open Medicine*, vol. 14, no. 1, pp. 711–718, 2019.

[5] H. Saeidi, J. D. Opfermann, M. Kam, S. Wei, S. Léonard, M. H. Hsieh, J. U. Kang, and A. Krieger, "Autonomous robotic laparoscopic surgery for intestinal anastomosis," *Sci. Rob.*, vol. 7, no. 62, p. eabj2908, 2022.

[6] A. Kuntz, M. Emerson, T. E. Ertop, I. Fried, M. Fu, J. Hoelscher, M. Rox, J. Akulian, E. A. Gillaspie, Y. Z. Lee *et al.*, "Autonomous medical needle steering in vivo," *Sci. Rob.*, vol. 8, no. 82, p. eadf7614, 2023.

[7] H. Alemzadeh, J. Raman, N. Leveson, Z. Kalbarczyk, and R. K. Iyer, "Adverse events in robotic surgery: a retrospective study of 14 years of fda data," *PloS One*, vol. 11, no. 4, p. e0151470, 2016.

[8] R. D. Jara, A. D. Guerrón, and D. Portenier, "Complications of robotic surgery," *Surgical Clinics*, vol. 100, no. 2, pp. 461–468, 2020.

[9] A. S. Zelivianskaia, S. E. Bradley, and V. V. Morozov, "Best practices for repair of iatrogenic bladder injury," *AJOG Global Reports*, vol. 2, no. 3, p. 100062, 2022. [Online]. Available: https://www.sciencedirect.com/science/article/pii/S2666577822000132

[10] G. Romero-Velez, I. Robles, J. Jiménez, C. Cabrera, R. Luengas, D. Portenier, and M. Kroh, "Robotic magnetic surgery: Results from the first prospective clinical trial," *Ann. Surg.*, vol. 3, no. 4, p. e225, 2022.

[11] R. Dreyfus, Q. Boehler, S. Lyttle, P. Gruber, J. Lussi, C. Chautems, S. Gervasoni, J. Berberat, D. Seibold, N. Ochsenbein-Kölble *et al.*, "Dexterous helical magnetic robot for improved endovascular access," *Sci. Rob.*, vol. 9, no. 87, p. eadh0298, 2024.

[12] L. O. Mair, X. Liu, B. Dandamudi, K. Jain, S. Chowdhury, J. Weed, Y. Diaz-Mercado, I. N. Weinberg, and A. Krieger, "Magnetosuture: Tetherless manipulation of suture needles," *IEEE Trans. Med. Rob. Bionics*, vol. 2, no. 2, pp. 206–215, 2020.

[13] M. Fan, X. Liu, K. Jain, D. Lerner, L. O. Mair, I. N. Weinberg, Y. Diaz-Mercado, and A. Krieger, "Towards autonomous control of magnetic suture needles," in *2020 IEEE/RSJ International Conference on Intelligent Robots and Systems (IROS)*. IEEE, 2020, pp. 2935–2942.

[14] W. Pryor, Y. Barnoy, S. Raval, X. Liu, L. Mair, D. Lerner, O. Erin, G. D. Hager, Y. Diaz-Mercado, and A. Krieger, "Localization and control of magnetic suture needles in cluttered surgical site with blood and tissue," in *2021 IEEE/RSJ International Conference on Intelligent Robots and Systems (IROS)*. IEEE, 2021, pp. 524–531.

[15] L. O. Mair, S. Chowdhury, X. Liu, O. Erin, O. Udalov, S. Raval, B. Johnson, S. Jafari, D. J. Cappelleri, Y. Diaz-Mercado *et al.*, "Going hands-free: Magnetosuture™ for untethered guided needle penetration of human tissue ex vivo," *Robotics*, vol. 10, no. 4, p. 129, 2021.

[16] J. Leclerc, A. Ramakrishnan, N. V. Tsekos, and A. T. Becker, "Magnetic hammer actuation for tissue penetration using a millirobot," *IEEE Rob. Autom. Lett.*, vol. 3, no. 1, pp. 403–410, 2017.

[17] O. Erin, X. Liu, J. Ge, J. Opfermann, Y. Barnoy, L. O. Mair, J. U. Kang, W. Gensheimer, I. N. Weinberg, Y. Diaz-Mercado *et al.*, "Overcoming the force limitations of magnetic robotic surgery: Magnetic pulse actuated collisions for tissue-penetrating-needle for tetherless interventions," *Adv. Intell. Syst.*, vol. 4, no. 6, p. 2200072, 2022.

[18] O. Erin, X. Chen, A. Bell, S. Raval, T. Schwehr, X. Liu, P. Addepalli, L. O. Mair, I. N. Weinberg, Y. Diaz-Mercado *et al.*, "Strong magnetic actuation system with enhanced field articulation through stacks of individually addressed coils," *Scientific Reports*, vol. 14, no. 1, p. 23123, 2024.

[19] X. Chen, A. Bhattacharjee, L. O. Mair, S. Raval, P. Addepalli, O. Erin, A. Bell, Y. Diaz-Mercado, and A. Krieger, "Mitigating singularities in control of magnetic capsule endoscopes using a novel nested electromagnetic coil system," *J. Med. Rob. Res.*, 2024.

[20] K. Alam, J. Umer, M. Iqbal, and A. Hasan, "Measurements of elastic properties of biological hydrogels using atomic force microscopy," *Journal of Physics: Conference Series*, vol. 1455, p. 012012, 2020, international Conference On Innovations In Nanomaterials & Nanotechnology 2019, 16-17 November 2019, Bangkok, Thailand. Open access article.

[21] P. Bjerle, "Tension, stress and modulus of elasticity of the urinary bladder wall," *Acta Physiologica Scandinavica*, vol. 92, no. 4, pp. 488–495, 1974. [Online]. Available: https://doi.org/10.1111/j.1748-1716.1974.tb05770.x

[22] M. Kim, S. Im, I. Park, D. Kim, E. S. Kim, J. Joseph, and J. Yoon, "Fabrication of agar-based tissue-mimicking phantom for the technical evaluation of biomedical optical imaging systems," *Curr. Appl Phys.*, vol. 61, pp. 80–85, 2024.

[23] MathWorks, "Segmentanythingmodel," 2024, accessed: 2024-09-14. [Online]. Available: https://www.mathworks.com/help/images/ref/segmentanythingmodel.html